Accepted Manuscript

Title: A sustainable multi-function biomorphic material for pollution remediation or UV absorption: Aerosol assisted preparation of highly porous ZnO-based materials from cork templates

Authors: Alessandra Quarta, Rui M. Novais, Simona Bettini, Michele Iafisco, Rob C. Pullar, Clara Piccirillo

PII: S2213-3437(19)30059-4
DOI: https://doi.org/10.1016/j.jece.2019.102936
Article Number: 102936

Reference: JECE 102936

To appear in:

Received date: 29 October 2018
Revised date: 10 January 2019
Accepted date: 1 February 2019

Please cite this article as: Quarta A, Novais RM, Bettini S, Iafisco M, Pullar RC, Piccirillo C, A sustainable multi-function biomorphic material for pollution remediation or UV absorption: Aerosol assisted preparation of highly porous ZnO-based materials from cork templates, *Journal of Environmental Chemical Engineering* (2019), https://doi.org/10.1016/j.jece.2019.102936

A sustainable multi-function biomorphic material for pollution remediation or UV absorption: Aerosol assisted preparation of highly porous ZnO-based materials from cork templates

Alessandra Quarta,[1] Rui M. Novais,[2] Simona Bettini,[3] Michele Iafisco,[4] Rob C. Pullar,[2] Clara Piccirillo[1]*

[1]: CNR NANOTEC, Institute of Nanotechnology, Campus Ecoteckne, Lecce, Italy

[2]: Department of Engineering of Materials and Ceramics / CICECO – Aveiro Institute of Materials, University of Aveiro, Aveiro, Portugal

[3]: Department of Innovation Engineering, Campus Ecoteckne, Lecce, Italy

[4]: Institute of Science and Technology for Ceramics (ISTEC), National Research Council (CNR), Faenza (RA), Italy

*Corresponding author, email: clara.piccirillo@nanotec.cnr.it

Graphical abstract

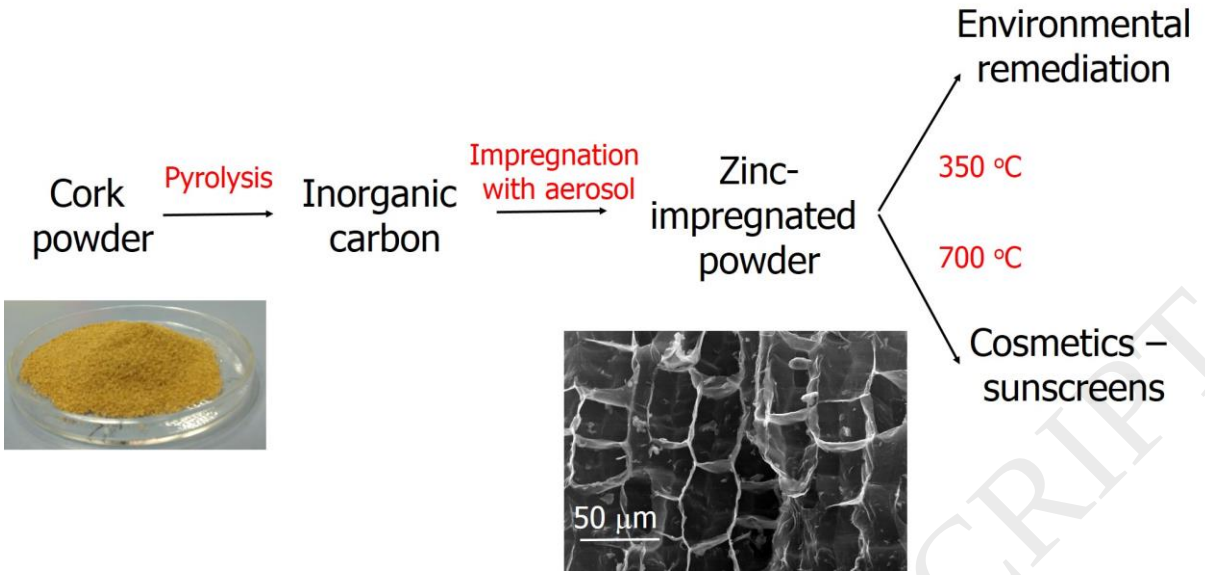

Abstract

For the first time, highly porous ZnO-based biomorphic materials were synthesised using cork as a natural sustainable template. In the first step, waste cork powder was pyrolysed and converted into inorganic carbon. This template was then infiltrated using a novel approach employing an aerosol of zinc-containing solutions. The infiltrated powders were calcined to convert the precursors into zinc oxide. Depending on temperature, these could form either a ZnO-graphite composite material, or pure ZnO. Their morphology, porosity, microstructure and composition were characterised; their optical band gap energies, ability to adsorb and photodegrade organic pollutants and UV absorption were also assessed. When heated to 350 °C they maintained the 3D porous cork structure, producing a graphite-containing composite material, with both physical adsorption and photocatalytic activity (Eg = 3.19 eV), suitable for environmental remediation. When heated to 700 °C, the powders were pure ZnO (no graphite), and they absorbed in the UV region, hence suitable for use as sunscreen. Doped ZnO ecoceramics were also produced, using silver and aluminium. An addition of 1 mol% Ag

improved photocatalysis under solar light. Conversely, adding 2 mol% Al and calcining at 700 ºC deactivated photocatalysis, but maintained strong UV absorption, producing a safer sunscreen material (no generation of free radicals). This is the first time that photocatalytic or UV absorption properties of any wood-derived biomorphic material or ecoceramic have been reported.

Keywords: biomorphic/ecoceramic; zinc oxide; aerosol; photocatalyst, sunscreen.

1. Introduction

Zinc oxide (ZnO) nanostructures are materials with interesting properties and potential applications in many different fields. Due to its biocompatibility, ZnO is widely used in biomedicine [1], and its optical properties (strong absorbance in the UV region) also make the material suitable for use as a sunscreen filter – in fact, ZnO is used in many commercial products as an inorganic sunscreen, together with TiO_2 [2].

However, although very effective as sunscreen filter, there is concern regarding its use due to its capability to generate free radicals and/or Reactive Oxygen Species (ROS) under light irradiation. In its more stable form of hexagonal wurtzite, ZnO is a direct wide band gap semiconductor, with a bang gap energy (E_g) of 3.37 eV (λ = 368 nm). This makes it a very good photocatalyst, which can be used for photodegradation of organic pollutants, as well as for light induced bacterial inactivation [3,4]. The photocatalytic performance of ZnO can be enhanced by the insertion of dopants inside the lattice; noble metals such as silver, gold or palladium, for instance, led to an increase of the photoactivity [5]. Higher photocatalytic efficiency can also be achieved considering composite heterostructures, in which ZnO is combined with noble metal nanoparticles such as Ag or Au [6,7]. Because of these properties, ZnO-based heterostructures can have the potential to be used for environmental remediation [8].

Although some elements can enhance the photocatalytic behaviour, other dopants may have the opposite effect, i.e. inhibiting ROS formation or, once they are formed, favouring their recombination; aluminium and iron, for instance, were shown to have this effect [2,9]. This could be a very valuable tool to develop a safer, non-photocatalytic ZnO powder which is still usable as sunscreen.

The morphology of a material, both at the micrometric and nanometric scale, is a parameter playing a crucial role for such properties. In particular, a hierarchical structure, with

different levels of porosity, can have a beneficial effect on the photocatalytic and absorbing performance of a material. The use of appropriate template agents is often considered, to achieve specific features/characteristics.

In recent years there has been a growing interest in exploring natural template agents, to obtain biomorphic materials, i.e. synthetic materials which maintain the same structure of the natural templates. Different kind of wood, vegetable fibres, leaves and biopolymers have been employed (amongst others) as templates, to make a range of ceramic materials [10]. A common and effective way to prepare biomorphic ceramics is to pyrolyse the natural template using a relatively slow heating ramp in the absence of oxygen, to convert it into graphitic carbon which retains the same 3D structure of the original material. The carbon template is then successively infiltrated with appropriate chemical compounds, which can then form the desired ceramic [11]. Due to the sustainable nature of the natural templates, such materials are also known as ecoceramics (environmentally conscious ceramics) [12].

Amongst potential wood templates, cork (the bark of the evergreen oak *Quercus suberus L.*) is a particularly interesting option, for various reasons. The use of cork is sustainable, as the tree is not harmed during the harvesting of the bark (the harvesting is performed every 9-13 years). The main components of cork are suberin and lignins (about 45 and 22 %, respectively). Its microstructure is formed of prismatic cells with a hexagonal honeycomb shape in the radial direction, and a rectangular form in the transverse direction [13-14]. The cells have an average length and width of about 40-45 and 15-20 μm, respectively; the cell walls are about 1-1.5 μm thick, and they are crossed by channels with a diameter smaller than 100 nm [14].

Due to its interesting morphology and structure, several cork-based composite materials were developed for different technological applications [15]. However, relatively few studies have been performed on the use of cork as a template agent, to prepare biomorphic materials or

ecoceramics; literature reports hexagonal ferrite and SiC ceramics made from pyrolysed cork [16-18]. In both cases, the cork-derived 3D graphite template was infiltrated using liquid media (liquid reagent and/or solution).

In this work, we describe the synthesis of ZnO-based materials using cork as a template. Although the first step of the process was the same as that previously employed (i.e. pyrolysis for conversion into inorganic carbon), the infiltration was performed using a new approach, with an aerosol of a zinc-containing solution. This is the first time that any kind of wood-templated biomorphic ceramics have been produced using an aerosol for impregnation.

The prepared materials were characterised with different techniques (XRD, SEM, DTA/TGA, FTIR, Raman), to determine their morphology/structure and composition. Their UV-Vis spectra, optical band gap energies and photocatalytic activity were also assessed. The use of dopants was also considered, to evaluate whether this method was suitable to prepare doped powders; the chosen elements were silver and aluminium, considered as model dopants because they can lead to either an increase (Ag) or to a decrease (Al) of the photocatalytic properties.

2. Materials and methods

2.1 Pyrolysis of cork powder

Cork powder was supplied by Amorim Cork Composite (Mozelos, PT). The cork had been immersed in hot water (100 ºC), which is a typical industrial pre-treatment performed on cork to expand the cork cells, creating a more regular and uniform structure [19], and it is known as boiled cork. The cork powder used was a waste material, with a stated particle size of around 200-400 μm. The powder was used without any further treatment.

The powder was pyrolysed at 900 ºC using a Thermal Technology 1000-3650-FP20 Vacuum Furnace; an oxygen-free nitrogen gas flow was flushed inside the furnace during the whole process. The following cycle was used: i) 5 ºC/min heating rate up to 150 ºC; (ii) 10 ºC/min heating rate up to 700 ºC; iii) 1 ºC/min heating rate up to 900 ºC: iv) 30 min dwell time at this temperature; and (v) cooling (at 10 ºC/min) to room temperature.

2.2 Infiltration of the pyrolysed powder

The infiltration of the pyrolysed cork powder was performed using the experimental apparatus shown in Figure 1 – a modified rotary evaporator connected to an aerosol generator.

The solution containing the precursors was placed into a flask. The aerosol was generated with an Asiamist 1308 ultrasonic humidifier (frequency 20 kHz), and it was transported into the flask containing the pyrolysed cork through a flow of inert gas (N_2). The contact between the aerosol and the powder was achieved by rotating the flask at an appropriate speed. When the condensation of the aerosol took place, the liquid was removed via evaporation.

For all experiments, methanol was used as solvent, as it is known to be a suitable solvent to form an aerosol [20]. Moreover, methanol has also previously been used in aerosol-based synthesis to prepare ZnO, in the form of both powder and thin films [21]. To prepare single-phase ZnO samples, both zinc acetate ($Zn(CO_2CH_3)_2 \cdot 2H_2O$) and nitrate ($Zn(NO_3)_2 \cdot 9H_2O$) were used as precursors; samples were named **ZnAc** and **ZnNit** respectively. For both zinc sources, the concentration was 45 mM.

For doped samples, $AgNO_3$ and $Al(NO_3)_3 \cdot 9H_2O$ were used for Ag and Al doping, the samples being named **ZnAg** and **ZnAl**, respectively. Their concentration was calculated to achieve the selected molar ratio between the dopant and the zinc; zinc nitrate was always used as a Zn precursor to prepare doped samples.

For all experiments, 0.025 g of pyrolysed cork powder was used, and it was assumed that it consisted only of carbon. The amount of zinc was calculated considering a mole amount of about 25 % in excess than that of carbon; this corresponded to 60 ml of solution. In some cases, more than one infiltration cycle was performed.

At the end of each infiltration, the powder was dried overnight at 60 ^{o}C, and successively either infiltrated again or calcined at the desired temperature (350-700 ^{o}C).

2.3 Characterisation of the materials

The phase composition of the samples was determined through X-ray Diffraction (XRD), with a Rigaku Geigerflex D/max C-series, with Cu K-α radiation. The diffraction patterns were acquired at a speed of 3^{o}/min, with a step 0.02^{o}, between 20 and 70 ^{o}. Phases were identified using the JCPDF standard file 01-080-4199 for ZnO and 00-004-0783 for metallic Ag; the crystallite size of the powders was calculated considering the full width half maximum (FWHM) of the (101) peak at 2θ = 36.26 of the ZnO pattern. For Al-doped samples, aluminium concentration was determined using an Inductively Coupled Plasma Atomic Emission (ICP-OES) spectrometer (Liberty 200; Varian); the powders were dissolved in 1 wt% ultrapure HNO_3. The morphology of the samples was studied using Scanning Electron Microscopy (SEM) (Carl Zeiss Merlin, equipped with a Gemini II column and an integrated high efficiency In-lens for secondary electrons). Prior to the analysis, samples were sputtered with gold.

Thermogravimetric and Differential Thermal Analysis (TGA/DTA) were performed using SDT Q600 equipment (TA Instruments), with an air flow rate of 100 ml/min and a heat ramp of 5 ^{o}C/min. FTIR spectra (64 scans for each spectrum) were acquired using a PerkinElmer Spectrum One Fourier Transform spectrophotometer with an ATR plate and a resolution of 4 cm^{-1}, Raman spectra were taken with A Horiba MicroRaman Xplora (laser at 532 nm, power 0.125 mW cm^{-2}), while for UV-Vis spectra a Perkin Elmer Lambda 1050, with

a 150 mm InGaAs Integrating Sphere, was used. The measurements were taken in reflection mode. Data were converted into the Kubelka-Munk function with the equation:

$$K = \frac{(1-R)^2}{2R}$$

where R is the reflectance, while K is the Kubelka absorption coefficient.

The value of the band gap of the material was calculated considering the first derivative curve of the spectrum.

The surface area of the samples was measured by a Micrometrics Gemini VII Surface Area Analyzer (Micrometrics Instruments Corp., Norcross, GA, USA), using N_2 as the adsorbate gas, and outgassing the samples at 120 ºC. The adsorption/desorption isotherms were measured, and the specific surface area (SSA) was calculated by the BET method.

2.4 Test of the photocatalytic activity

The photocatalytic activity of the samples was assessed by monitoring the decrease in the concentration of methylene blue (MB) dye over a period of 30 minutes. The tests were performed using a 150 W Xe lamp (LOT Oriel Gmbh) as an artificial sunlight source; the light was at 10 cm distance from the samples, and a filter reducing the transmittance to 10 % of the original value was used. Parallel tests were also performed with no light irradiation, in the dark, for the same length of time, to take into account the adsorption of the dye on the surface of the material. For the all experiments, a powder concentration of 0.5 g/L was used. The change of MB concentration was monitored with UV-Vis spectroscopy, using a Varian Cary300SCAN spectrometer; the area under the adsorption curve was integrated over the 400-800 nm range. The initial MB concentration was that corresponding to a maximum adsorption (λ = 662 nm) of about 1 unit of absorbance.

For selected sample(s), additional experiments were performed to understand the photodegradation mechanism and to check the reusability of the material for more than one cycle. Regarding the photodegradation mechanism, some ROS scavengers were added to the MB solution; more specifically, ethylendiamine tetracetic acid (EDTA), isopropanol (IPA) and 1,4-benzoquinone (PBQ) were added as scavengers for holes h^+, hydroxyl $^{\bullet}OH$ and superoxide $^{\bullet}O_2^-$ radicals, respectively [22]. The decrease in the MB concentration in the presence of each scavenger was compared to that with no scavenger. To estimate the reusability of the material, at the end of the experiment, the used powder was separated from the solution, washed with distilled water and dried at 60 ^{o}C. No further thermal or chemical regeneration was carried out. The same powder was then reused for a successive experiment. These tests were performed both in the dark and under irradiation, to check whether the possible change in the MB decrease concentration was due to either a difference in the adsorption, or in the photocatalysis.

3. Results and discussion

3.1 Infiltration of the pyrolysed cork

Aerosol-based systems have never previously been used to infiltrate cork, or any other natural materials, to make biomorphic materials or ecoceramics. Because of this, preliminary experiments were performed to assess whether an aerosol was effective or not in infiltrating the pyrolysed cork powder. To do this, the infiltration process was repeated a different number of times – from 1 to 3 - and the weight uptake of the powder was measured; this was calculated as the weight of the infiltrated dry powder divided by the weight of the original powder used

(0.025 g). The results are reported in Table 1; the values are an average of three experiments, with the associated standard deviation.

It can be seen that in all cases a significant increase in the weight of the powder occurred; this confirms that the powder is infiltrated into the pyrolysed cork by the aerosol. The droplets constituting the aerosol can have different dimensions, depending on the physical characteristics of the solution [23] and the frequency of the ultrasound generator used. With methanol as solvent and the present experimental apparatus, the droplets' diameter is about 50-70 μm, depending on the nature and concentration of the solutes [24]. Based on this, it can be stated that the aerosol droplets are much larger than the pores of the walls of the cork cells, which are below 100 nm [14]; despite this, however, the infiltration is effective, indicating that the drops are able to wet the surface and penetrate into the pores.

Comparing the values observed with the different precursors, it can be seen that the weight increase is higher with zinc nitrate than with zinc acetate. With the acetate, there is no significant difference in the weight uptake after 2 and 3 infiltration cycles, and the maximum value achievable is around 7 times the weight of the powder used. With nitrate, on the contrary, higher values were observed (up to 14 times the weight), and smaller differences were seen between the different replicates (smaller values of the standard deviation). Moreover, after 3 cycles, the system still did not appear to have reached saturation.

The higher efficiency and reproducibility of the nitrate indicate that the zinc counter ion plays a key role in the aerosol infiltration process; indeed, literature data report that aerosol-prepared ZnO coatings showed different characteristics and properties according to the counter ion used [20]. Considering in particular our study, the interactions with the surface of the graphite powder can be different, thus affecting the infiltration. The use of methanol as a solvent, although suitable for aerosol processes, makes the system quite complex and its

behaviour difficult to predict, due to the presence in its structure of both hydrophobic and hydrophilic functional groups. Literature reports the interaction of Zn^{2+} ion with methanol [25], but no details are given on the possible effects of the negative ion(s).

3.2 Conversion of the infiltrated powder into ZnO

The infiltrated powders were successively calcined in air to convert the zinc precursor into zinc oxide (ZnO). To better understand the conversion process, TGA analyses were performed on the powder infiltrated with either zinc acetate or nitrate; a comparison with the untreated pyrolysed cork powder was also made. The TGA curves for all three samples are shown in Figure 2(a). The first derivatives of the curves are reported in Figure 2(b) for the untreated powder, and Figure 2(c) for the infiltrated ones – the various weight loss steps are identified more clearly in these first derivative plots.

The TGA data for the pyrolysed pure cork powder were recently published [26]; they were reported here again to make easier a comparison with the two infiltrated systems. From the TGA curve, a complete weight loss (100 %) can be observed for temperatures just below 500 ^{o}C. The first derivative curve (Figure 2(b)) shows a first small weight loss for $T < 100$ ^{o}C, which could be associated with the desorption of water and other molecules present on the surface of the powder. A much greater loss was seen for $350 < T < 500$ ^{o}C, which corresponds to the combustion of the carbon. Since this is by far the main element the powder consists of, it is reasonable to have a virtually complete weight loss associated with it.

The curves for the infiltrated powders are very different from that of the untreated one. In fact, in both cases, no complete weight loss is observed. This confirms the presence of different elements other than carbon, introduced during the infiltration process. The overall weight loss was greater for the powder treated with zinc acetate than nitrate (residual weights were about 13% and 22%, respectively); this is in agreement with the data of Table 1, showing

higher zinc uptake when the nitrate precursor was used. The first derivative curves (Figure 2(c)) show that there are more significant differences between the two salts.

In the case of zinc acetate, only two main weight losses can be observed – the first one for 200 < T < 250 ^{o}C, while the second one is for 250 < T < 310 ^{o}C, this second one being greater than the first one. The first peak can be associated with the loss of the organic fragment derived from the acetate anion, as well as the solvent, while the second one is likely to be the combustion of most of the graphitic carbon. Two more small peaks are also present, for temperatures just below 100 ^{o}C and about 460 ^{o}C; the first one can be related to the desorption of the adsorbed water, while the second to the combustion of residual carbon not yet eliminated at lower temperatures. It is interesting to note that, in the presence of the zinc, the majority of the carbon combusts at a lower temperature than for the untreated powder (see Figure 2(b)).

For the zinc nitrate, a very different profile can be observed; the first derivative curve shows a greater number of peaks, with smaller and similar intensities. This indicates that several reactions take place during the heating – this is likely to be due to the presence of different nitrate-derived ions (e.g. nitrate, nitrite, etc.), as well as to the interactions between these ions and the carbon. The first peak, just below 100 ^{o}C, is similar to that observed for the zinc acetate, which is desorption of the water. It is interesting to note that, in this case, the peak is stronger, indicating that more water gets adsorbed onto the surface of the powder with the zinc nitrate treatment. Two more peaks can be seen at about 135 and 160 ^{o}C; as these were not observed for the acetate, it is reasonable to say that these are associated with the release of nitrogen-containing ions/species. For T < 250 ^{o}C, a further peak is present, similar to that observed for the acetate, due to the release of the organic carbon. Finally, two more peaks are detected for 400 < T < 500 ^{o}C, related to the combustion of the graphitic carbon.

Figure 2(d) compares the DTA curves of the three systems. In the case of the untreated powder, the main peak is a strongly exothermic one at 450-500 ^{o}C, due to the combustion of the graphitic carbon. For the acetate-infiltrated powder, a first, broad endothermic peak is observed for T > 50 ^{o}C, which is related to desorption of the water; this is followed by a very sharp endothermic peak at about 250 ^{o}C, corresponding to the release of the organic carbon. Since this peak is endothermic, it can be stated that the process is not a combustion, but more like a desorption combined with the breaking of chemical bonds. For higher temperatures (> 300 ^{o}C), the exothermic peaks associated with the carbon combustion can be observed; it is interesting to note that, although the bulk of the weight loss takes place at 300 ^{o}C, the heat is released in two different steps, at about 300 and 450 ^{o}C. Finally, some broad signals can be seen at T > 600 ^{o}C; as no weight change was observed by the TGA, it is likely that this is due to rearrangements of the ZnO lattice.

The curve of the zinc nitrate powder, on the other hand, showed a much stronger endothermic peak due to the desorption of water; this is in agreement with the higher weight loss observed by the TGA (Figure 2(a) and 2(c)). The peak at T < 160 ^{o}C is due to the release of nitrate-derived fragments; since the signal is exothermic, it is likely a combustion of these species. The endothermic release of the organic carbon is observed for T > 200 ^{o}C, similar to that seen for the acetate-infiltrated powder; in this case, however, the peak is weaker, due to the lower carbon content (no added acetate groups). Successively, the peaks associated with the combustion of the graphitic carbon (exothermic) are present for 400 < T < 500 ^{o}C; as already observed for the zinc acetate system, also here two distinct exothermic peaks are present. It is interesting to note that, although more energy is released in the combustion for the nitrate sample (maximum value about 15 μV), this process takes place at a higher temperature than for the acetate (T > 400 ^{o}C vs. T > 300 ^{o}C).

3.3 Characterisation of the calcined samples

Different numbers of infiltration cycles and calcination conditions were explored to assess the possible effect(s) on the characteristics of the prepared ZnO powders. The full list of the prepared samples, with the corresponding preparation conditions, is reported in Table 2. In all cases a slow heating ramp was used (1 ^{o}C/min), to preserve the cork 3D structure. At the same time, however, different calcination temperatures as well as calcination times were considered. SEM micrographs were taken to assess under which conditions the cork structure was actually preserved, and to study the morphology of the powders at micrometric scale. For reference and comparison, micrographs of the cork powder before and after the pyrolysis are reported in the Supplementary Information SI (Figure S1(a) and S1(b) respectively).

Although the ramp used in the calcination was different from that used in the TGA-DTA experiments (1 vs. 5 ^{o}C/min), the TGA-DTA data described above were used as a guide to select the calcination temperatures. First calcination experiments were performed at 350 ^{o}C and 400 ^{o}C, with 1 hour calcination time; at 350 ^{o}C it was likely that the samples would contain some residual graphitic carbon, while at 400 ^{o}C much more (if not all) of the graphite would have been burnt off.

Figures 3(a) and 3(b) show the SEM images for samples prepared from zinc acetate at 350 ^{o}C, with two and three infiltration cycles, respectively. With two infiltration cycles (**ZnAc1**), it can be seen that the cork structure is mainly preserved, and the typical honeycomb-shaped cells can be observed. With three cycles (**ZnAc2**), the shape of the cells can still be seen, although the forms are less defined. These images seem to indicate that the third infiltration cycle caused an additional loading of the cork-derived powder, which saturated the cell walls, and began partially filling up the voids within the cells themselves. Micrographs taken at higher magnifications (Figure 3(e) and 3(f)) show that both samples have a nano-

structured morphology, with rounded particles having an average diameter of about 30-50 nm. For **ZnAc2**, however, these small particles aggregate into larger rounded structures (about 300 nm).

Increasing the calcination temperature to 400 ^{o}C causes significant changes in morphology. In fact, in both **ZnAc3** and **ZnAc4** the structure of the cork is not present anymore. In **ZnAc3** (Figure 3(c)), the highlighted features could be remaining parts of the cell walls damaged during the combustion, while for **ZnAc4** (Figure 3(d)) the morphology of the powder is very compact, with no resemblance at all to the cell-shaped cork. Looking at the morphology at a higher magnification (Figure 3(g) and 3(h)), in these samples rounded nanoparticles can also be observed, although slightly larger than those observed in the samples calcined at 350 ^{o}C.

Figure 4 shows the images for the samples prepared under the same conditions, but using zinc nitrate as a precursor. As observed with the acetate, the nitrate powders calcined at 350 ^{o}C (Figure 4(a) and 4(b)) also have the typical 3D cork structure. Considering in particular the sample prepared with 3 infiltrations (**ZnNit2**, Figure 4(b)), it can be seen that the shape of the cells is better defined than the corresponding sample prepared with acetate (Figure 3(b)). This is in agreement with the data of Table 1, indicating that after 3 nitrate infiltrations, the system has not yet reached saturation. Figure 4(e) (**ZnNit1** at larger magnification) shows the growth of the material inside the cell, and overall, the structure is more irregular than that of **ZnAc1**. A more irregular morphology can also be observed for **ZnNit2** (Figure 4(f)); indeed, although some spherical nanosized particles are present, larger and elongated shapes can also be detected.

The powders calcined at 400 ^{o}C (Figures 4(c) and 4(d)) do not maintain the 3D cork structure, similar to that observed for those prepared with zinc acetate. However, both **ZnNit3** and **ZnNit4** show some empty voids, which may correspond to the cork cells. The images with

higher magnification (Figures 4(g) and 4(h)) show a nano-structured material, with particles with more elongated shape, and of about 50-70 nm length.

The loss of the cork structure for temperatures above 400 ^{o}C is not in agreement with previous work on cork-derived ceramics; indeed, literature reports that pyrolysed cork powder infiltrated with a hexagonal ferrite precursor sol maintained the characteristic 3D cork structure in the final ceramic for calcinations of up to 1200 ^{o}C [16]. A possible reason for this difference is that in the past an aqueous sol was used, while in the present work methanol is employed as solvent - it is possible that the heat released in the presence of the organic solvent is greater, causing damage to the 3D structure. Also, although the sol was stabilised by nitrate ions [16], they were at a quantity much lower than that of the nitrate or acetate ions contained in the salt solutions used here, and their exothermic removal could also be damaging to the cork microstructure. In the work with the hexagonal ferrite sol, no TGA-DTA data are reported for the calcination of the infiltrated powder; because of this, it is difficult to perform a proper comparison.

Even when the 3D cork structure is not maintained (400 ^{o}C), however, the resulting materials have an interesting morphology, showing the formation of ordered nanocrystals. This indicates that cork acts as a good growth / nucleation substrate, and this is particularly true for the samples prepared using zinc acetate, which show smaller and more regular particles. The fact that the infiltration takes place through small aerosol droplets (instead of "continuous" liquid solution) may also play a role in determining the growth mechanisms.

Further experiments were performed at 350 ^{o}C, but for longer calcination times of 3, 5 and 7 hours; this was carried out to try to maintain the 3D structure while reducing the graphite content. The micrographs of these samples are reported in Figure S2 in the SI. When zinc acetate was used as a precursor, the cork structure was preserved to a limited extent. For a 3

hour calcination (**ZnAc5**, Figure S2(a)), some residual cork cells may still be observed; for longer times, however, the walls of the cells appear to have been damaged (**ZnAc6** and **ZnAc7**, Figure S2(b) and (c), respectively). With nitrate, on the other hand, the cork structure seems to be better maintained (Figure S2(e), S2(f) and S2(g)), and even for the longest calcination time of 7 hours, some cork-like cells can still be observed (**ZnNit7**, Figure S2(g)). It has to be highlighted, however, that some of the cells appear to be open, as if the side walls were not affected, but the rear wall of the cell was. This indicates that the resulting materials show a higher level of open porosity / connectivity, and this property could be useful for applications in several fields, including energy storage, catalysis and biomedicine.

Overall, it seems that the use of zinc nitrate is more effective in preserving the 3D cork structure; this could be due to the fact that, as stated above, the majority of the combustion heat is released at higher temperatures in the powder infiltrated with zinc nitrate (see Figure 2).

ZnNit1 was also recalcined at 700 ^{o}C (**ZnNit1a**), and its morphology is shown in Figure S2(d). It can be seen that the higher calcination temperature led to the damage of the 3D cork structure; however, some open voids, which resemble the shape of the cork cells, are present. **ZnNit1a** morphology shows grains on average larger than for **ZnNit1** (> 100 nm), which is expected due to the higher temperature used.

All samples were analysed by XRD, to determine the phase composition. In all cases ZnO in wurstite form was detected, with no other phase present. Some selected diffraction patterns are reported as examples in Figure 5 (a-d), while the crystallite sizes are listed in Table 3. For all samples, no preferred orientation was observed, regardless of the precursor and the calcination conditions; this can be explained considering that, according to literature, preferred orientation is more likely to take place when additives and/or surfactants are employed in the synthesis [13,27].

The preparation conditions, however, had a significant effect on the crystallinity of the powders. Considering the different precursors, it can be seen that crystallites are consistently larger when zinc nitrate is used (between 16-18 nm), compared to ~14 nm for zinc acetate (see Figure 5(a-d) and Table 3). This indicates that the negative counter ions affect not just the zinc uptake, but also the ZnO growth mechanism. As expected, an increase in the calcination temperature led to larger crystallite sizes. Such an increase can already be seen comparing samples prepared at 350 and 400 ^{o}C, even if it is not very large (Figure 5(b)), and it becomes ever more enhanced for calcination at 700 ^{o}C (about 30 % increase to >22 nm, Figure 5(c)). For the different calcination times at 350 ^{o}C, a trend (increase) with time can be seen when zinc nitrate is used; for acetate, however, no pattern can be detected. Overall, the crystallites are relatively small, indicating a lower degree of crystallinity, which could be due to the low calcination temperatures used (apart from **ZnNit1a**).

Adsorption isotherms and surface area measurements for some selected samples are shown in Figure 6. In can be seen that, despite the large variations in their surface area values, all samples exhibit a type IV isotherm typical of a porous material, with narrow hysteresis loops. This shows monolayer coverage in the initial increase, followed by subsequent multilayer coverage, with the hysteresis loop being caused by capillary condensation in mesopores (between 20 and 500 Å). These data show that the samples prepared here are different from the majority of activated carbons, which are generally microporous solids and for which the uptake only occurs as a monolayer in micropores (<20 Å), resulting in a type I isotherm, without the later multilayer adsorption or any hysteresis [28].

Looking at the isotherms, it can immediately be seen that **ZnAc1** had a much greater SSA (120.09 m^2/g) than the other samples, and **ZnNit1a** has the smallest, at only 7.64 m^2/g, indicating that heating the samples to 700 ^{o}C is highly detrimental to their surface area due to

the grain growth observed above. These results indicate that the acetate precursor results in significantly higher SSA that the nitrate when heated at 350 ºC / 1 h (120.09 vs. 48.28 m^2/g). The other samples all have much lower and comparable SSAs (21-24 m^2/g).

As we will show in section 3.4, these differences in surface area values contribute significantly to the absorption/photocatalytic properties of these materials.

To detect any possible residual organic matter present in the samples, either in graphitic or in a different form, FTIR spectra were acquired; Figure S3(a) shows the data for some selected samples. The spectrum for **ZnAc1**, for instance, shows a broad peak at about 1565 cm^{-1}, corresponding to the carbon-carbon double bond usually detected for graphite [29]. This is reasonable, since **ZnAc1** was calcined at 350 ºC and still contains some graphite. The fact that this was not detected in the XRD pattern indicates that its concentration is relatively low, below the technique's detection limit, and/or that it is not very crystalline. Increasing the temperature to 400 ºC, on the other hand, leads to graphite combustion; in fact, in the **ZnAc3** spectrum (blue line Figure S3(a)), the graphite peak disappears, while signals corresponding to carbon-oxygen bonds can be detected, in the 1410-1480 cm^{-1} region, as well as at about 875 cm^{-1} [30]. **ZnNit1a** shows similar features already highlighted for **ZnAc3**, even if the peaks are less intense. Although the FTIR technique is not quantitative, it is reasonable to assume that smaller quantities of residual carbon could be present in the material. All spectra show a very intense drift for $\nu < 580$ cm^{-1}, which is due to the presence of ZnO [31]. Residual graphitic carbon was also confirmed through Raman spectroscopy - as can be seen in Figure S4, the spectrum of the pyrolysed cork shows the characteristic peaks at about 1355 and 1580 cm^{-1} (D and G peaks respectively) [32]. The same signals can also be observed for sample **ZnAc2**, even if with much smaller intensities. The spectra of other samples showed similar features, with the intensities of the D and G peaks decreasing for increasing calcination temperatures and/or times.

Figure 7 reports the UV-Vis spectra of some selected samples, all showing the characteristic ZnO profile, with some absorbance in the UV and then a decrease towards the visible for $\lambda > 370$ nm [2]. Differences between the samples, however, can be observed. **ZnAc2**, for instance, shows a significant absorption in the visible range. This is confirmed by the fact that the sample is not white (the standard ZnO colour), but grey, due to some residual graphite as it was calcined at 350 ^{o}C (in agreement with FTIR data). For **ZnNit7**, on the other hand, graphite content is lower, as the calcination at 350 ^{o}C was more prolonged (7 hours), and because of this its absorbance in the visible is much lower, almost zero. The spectra of other samples, not reported here, showed similar features, i.e. different visible absorption according to the graphite content that, in turn, depends on the calcination temperature and duration. **ZnNit1a**, however, had a slightly different profile - it can be seen that it has higher absorbance in the UV, while absorbing almost nothing in the visible. Indeed, the powder has the characteristic white ZnO colour, as all graphite was removed at 700 ^{o}C. A sample with these properties could be effectively used as sunscreen. Moreover, in this sample, a much sharper decrease in the absorption curve can also be observed, which is in agreement with the higher degree of crystallinity of this sample.

The value of the band gap calculated from these spectra was around 3.19 eV. No significant differences were observed between the various samples, the only exception being **ZnNit1a**, showing higher a band gap of 3.27 eV. These values are lower than ZnO standard literature data (3.37 eV) [3]. It has to be highlighted, however, that for nanoscale materials this kind of property can vary according to their characteristics, as well as their preparation protocols and eventual preferred orientation. Indeed, literature reports ZnO nanopowders showing different band gap values, comparable to those observed here [33-35], and the dependence of E_g on the size of the particles was also reported [34].

3.4 Photocatalytic activity

The photocatalytic activity of some selected samples is shown in Figure 8(a); tests were performed monitoring the decrease in concentration of methylene blue dye (MB). As stated in the experimental section above, parallel experiments were performed in the dark, with no light irradiation, to assess the extent of the adsorption of the dye on the surface of the powder.

It can be seen that **ZnAc1** is that showing the greatest decrease in MB concentration. Considering the experiment carried out with no light irradiation, however, a significant proportion of the dye was not photodegraded, but adsorbed by the material (about 52 %). This is reasonable, since **ZnAc1** still contains some residual graphite, as shown above, and it is well known that graphite is a very powerful adsorber of organic molecules [36]. Moreover, as shown by the SEM image (Figure 3(a)), **ZnAc1** has a 3D structure resembling that of cork, and is, hence, very porous, which corresponds to a high adsorption property [36]; this sample also had the largest SSA (see Figure 6). Often cork-derived graphitic materials (not ceramics, as reported here) need activation to decrease their hydrophobicity and increase the adsorption performance [37]. In this case, however, the presence of a polarised material such as ZnO makes the material already quite hydrophilic, leading to greater adsorption efficiency. Literature data report that the combination of ZnO and graphite-based materials can be beneficial for treatment of pollutants, due to the synergistic effect of adsorption and photocatalysis. Yue [38], for instance, reported the use of a graphite/ZnO composite to adsorb and photodegrade spilled crude oil. Enhanced photocatalytic activity was also observed when ZnO/graphite nanowires were tested [39].

Comparing with the other zinc acetate-derived cork-based ceramics reported here, it can be seen that both higher calcination temperatures and longer calcination times correspond to worse performances. Indeed, **ZnAc3** (400 ^{o}C) showed both inferior adsorption (10 vs. 52 %)

and photocatalytic degradation (11 vs. 18 %). This decrease in the adsorption can be explained considering the lower graphite content, the less porous 3D structure (as the cork structure is not maintained, see Figure 3(c)) and the lower SSA. Regarding the photocatalytic activity, the lower efficiency can be explained considering both the reduced SSA and more irregular morphology at the nanoscale level (Figure 3(g)). For **ZnAc7**, both the adsorption and the photocatalytic activity are worse than **ZnAc1**, indicating that the longer calcination time is not an effective way to obtain materials with better photocatalytic characteristics, although it was superior to **ZnAc3**. This also suggests that although treatment at 350 ºC / 7 h was detrimental to the catalytic properties, it was less than harmful than only 1 h at 400 ºC, as shown by the adsorption and photocatalysis data, as the performance of **ZnAc7** is still better than **ZnAc3**. The other samples prepared from zinc acetate under different conditions showed activity comparable to **ZnAc7** (data not shown).

For the samples prepared from zinc nitrate, results show some similarities to those of zinc acetate, but also some significant differences. The most effective sample is **ZnNit1**, which was prepared under the same conditions as **ZnAc1**, but with a different precursor. Both the adsorption and the photocatalytic activity, however, are lower than for **ZnAc1** (47 and 7 % respectively); one possible reason could be the microstructure of this sample (see SEM micrographs), as more irregular and larger particles were observed, which could affect the interaction with the molecules in solution. Moreover, **ZnNit1** also had a significantly lower BET SSA (see Figure 6). **ZnNit1a**, heated to 700 ºC / 1 h, had by far the lowest BET SAA and subsequently was the worst at adsorbing MB.

However, comparing all the different samples prepared with zinc nitrate, it can be seen that they all have comparable photoactivity (all samples degrade around 7 % of MB). This suggests that the different calcination conditions only have an effect on the adsorption capacity,

due to changes in the nature of the available micro- and meso porosity, but not on their ability to generate ROS under light. The other materials, not reported in Figure 8, showed performances comparable to those of **ZnNit6** and **ZnNit7**.

Tests of the photoactivity reported in literature are often performed using different experimental conditions (light irradiation, catalyst concentration, tested model pollutant(s), etc.); this makes it very difficult to compare the activity of these materials and other ZnO catalysts prepared with different protocols. A comparison of the mechanism of the photocatalysis, however, can be performed. This can be achieved by understanding which ROS were active during the photodegradation. To do this, experiments were performed using selected radical quenchers, i.e. EDTA, IPA and 1,4 benzoquinone; results are shown for sample **ZnAc1** (see Figure 8(b)). It can be seen that for all three quenchers, no significant difference is present for the tests performed in the dark - this indicates that none of these compounds have an effect on MB adsorption. Considering the photoactivity, however, different behaviours can be observed depending on the scavenger. When PBQ is used, comparable photocatalytic activity was observed. Using IPA, on the contrary, led to a significant decrease in the photocatalytic activity – from about 18% to 2%, i.e. almost no was photodegradation observed. Upon adding EDTA to the solution, an increase in the photocatalysis was observed (up to 26%).

The results of PBQ and IPA indicate that $\cdot O_2^-$ is not involved in the MB degradation, while the $\cdot$OH radical plays a crucial role in the photocatalytic mechanism. Comparing with ZnO literature, some studies report similar behaviour while others are different. $\cdot$OH radicals, for instance, were described as significant/dominant species, for both undoped and doped compounds [41-43], similar to what was observed in this work. $\cdot O_2^-$, on the other hand, has also been reported to be involved in the photocatalysis [41,44], in opposition to what reported here.

Such differences can be explained considering that the photocatalytic activity can be affected by several characteristics of the material: in particular, features such as morphology, dimension/shape of the crystals and possible presence of other phases can have a significant effect on the photodegradation mechanism. Data obtained with EDTA are different from existing literature, as an increase of the activity was never reported before; a decrease, on the contrary, was previously reported in several studies [41,43]. The unusual results obtained here suggest that, for cork-derived ZnO, holes do not play a role in the photodegradation. Although not observed for ZnO, a similar behaviour (i.e. an increase of the activity in the presence of a hole scavenger) was reported for different photocatalysts such as Fe_2O_3 [45]; further investigations are needed to explain this.

To test the reusability of the materials, repeated tests were performed with the same powder; results for sample **ZnAc1** are reported in Figure 8(c). It can be seen that in the second experiment, the overall decrease in the MB concentration is lower (from about 70% to 50% of the first run). Considering the separate contributions of the adsorption and photocatalysis, however, the decrease due to the photocatalytic activity does not change (18% in both cases), but it is the adsorption which shows a lower efficiency (from about 50% to 30%). A further decrease in the efficiency was also observed when the powder was used for the third time; the reduction, although observed for both photoactivity and adsorption, was smaller than that seen between the first and the second cycle.

The lower efficiency in the repeated tests can be explained considering that possibly the regeneration treatment of the powders was not the most appropriate for this kind of material. Indeed, washing and drying the powder is the standard protocol used to regenerate a photocatalyst, where limited adsorption takes place. For high surface area materials, however, where adsorption is the dominant feature, different regeneration protocols are generally

employed [46], examples including thermal or chemical treatments. For composite materials like the one considered in this study, the regeneration process needs to be tailored and optimised, and it will be the topic of further investigations.

Overall, these data demonstrate that the combination of ZnO and graphite can be effective in removing and degrading pollutants and, therefore, it has potential for environmental remediation. Considering in particular the use of cork as a templating agent, key elements are the morphology of the samples at the nanoscale, as well as the porous cork-like 3D microstructure.

3.5 Addition of dopants

Table 4 reports the list of the samples prepared with the addition of dopants. All samples were prepared with two infiltrations of the pyrolysed cork powder, while only zinc nitrate was used as the zinc precursor. For the Ag-doped sample the infiltrated materials were calcined at 350 ^{o}C, while for the aluminium doping a temperature of 700 ^{o}C was used. In all cases, a heating ramp of 1 ^{o}C/min was employed.

3.5.1 Addition of silver: photocatalytic enhancement

In doping with silver, this noble metal was used to increase the photocatalytic performance. Because of this, and based on the results shown in the previous section, zinc acetate would have been more suitable as a zinc precursor. Adding silver nitrate to the solution, however, leads to the formation of silver acetate, which has a very low methanol solubility; indeed, the formation of a white suspension was observed, confirming the precipitation. The presence of such solid particles would have been detrimental to the infiltration into the pyrolysed cork, due to the small size of the cork pores [14]. Consequently, all experiments were performed using a combination of zinc and silver nitrates. A calcination temperature of

350 ºC was chosen, as higher temperatures were shown to negatively affect the photocatalytic activity.

SEM micrographs of some selected samples are shown in Figure S5. It can be seen that both materials (**ZnAg1** and **ZnAg3**) kept the cork 3D structure, similar to that observed for the sample prepared under the same conditions but without silver (**ZnNit1**). This indicates that the presence of the noble metal does not affect the infiltration and calcination processes. The other samples showed similar results (images not shown).

XRD data of the Ag-doped samples are shown in Figure 5(e). It can be seen that an additional peak, corresponding to metallic silver, is present in all diffraction patterns, for 2θ = 38 º, indicating that not all silver is incorporated as a dopant, but that at least part of it forms a separate phase. This can be explained considering the larger Ag^{+} ionic radius in comparison to Zn^{2+} (1.26 vs. 0.74 Å) [5]. Looking at the values of the crystallite size, they are comparable to that of the undoped sample prepared under the same conditions (**ZnNit1**). However, a trend can be observed, as the crystallite size decreases with increasing Ag concentration. This change confirms that part of the silver is incorporated as a dopant into the ZnO lattice, with higher silver content corresponding to a decrease in the crystallinity of the materials; such a decrease was previously observed in other Ag-doped ZnO materials [47]. The presence of silver, on the other hand, did not lead to preferred orientation.

Figure S3(b) shows the FTIR spectrum of **ZnAg4**; comparing it with that of the undoped sample (Figure S3(a)), some differences can be observed. In fact, the signals ascribable to the C-O presence (i.e. 1410-1490 and 875 cm^{-1}) are more resolved than for the undoped sample calcined at 350 ºC (see **ZnAc1**). This would indicate that the combustion of the graphite is enhanced due to the presence of the noble metal.

UV spectra of some selected samples are reported in Figure 7(b); it can be seen that the absorption profile is similar to that observed for the single phase ZnO shown in Figure 7(a). An additional broad and small peak can be observed at about 500 nm; this corresponds to the Surface Plasmon Resonance (SPR) of metallic silver nanoparticles (NPs) [48]. Some work reports the SPR signal being at lower wavenumbers, i.e. about 450 nm [49], but it has to be highlighted that the position of the SPR band can vary depending on several parameters, including the chemical environment of the Ag NPs and their shape/dimensions [50-51].

The performance of the Ag-doped ZnO materials in decreasing the MB concentration is shown in Figure 8(d). It can be seen that the presence of the noble metal has an effect on both the adsorption and the photodegradation. **ZnAg1** and **ZnAg2** are both more effective than the undoped ZnO (see **ZnNit1**, Figure 8(a)), and with **ZnAg1**, in particular, a MB decrease of 80% is observed, while the effect of the photodegradation is about 17% – more than twice that of the undoped sample. Higher Ag content, on the other hand, led to a decrease in the efficacy of the material, as can be seen for **ZnAg3** and **ZnAg4**. As shown by SEM images, all samples exhibited a similar microstructure, with all retaining the original cork 3D shape. Therefore, the change in photocatalysis cannot be due to the morphology of the powders, but to the quantity of Ag present.

This is in agreement with literature data. As stated above, silver can have a beneficial effect on the photocatalysis [5,6], but a lower activity for higher Ag concentrations has been observed. However, the actual concentration "limit" above which Ag is detrimental can vary depending on the characteristics of the material. Vaiano et al. [49], for instance, report 1 % wt. (~0.75 mol%) being the most effective Ag content for ZnO, while for Jaramillo-Páez [52] Ag up to 5 % wt. was beneficial to the ZnO performance. Data of the present work are closer to that found by Vaiano, with 1 mol% addition of Ag (**ZnAg1**) being most effective. To explain

these data and differences, it has to be considered that many parameters can affect the photocatalytic activity; the morphology of the material surely plays a crucial role. Moreover, in some cases the presence of a higher amount of dopant can favour the recombination of the photogenerated charges [53].

3.5.2 Addition of aluminium: photocatalytic retardation

Aluminium doping was utilised to "kill" the photocatalytic capabilities of the material, to produce a potentially safer sunscreen UV absorber. For doping with aluminium, zinc nitrate was chosen as the precursor, as samples prepared from this salt already showed lower photocatalytic performance. The infiltrated powders were also calcined at 700 ^{o}C to obtain a material with no residual graphite left, and hence, also potentially usable as a sunscreen. SEM analysis (**ZnAl2**, Figure S5(c)) confirmed the loss of the cork structure already observed for the samples prepared at 700 ^{o}C; higher magnification images showed irregular and relatively large grains (> 150 nm), similar to those observed for **ZnNit1a**. These data indicate that, as already seen for Ag doping, the incorporation of aluminium did not significantly affect the infiltration and calcination processes.

XRD patterns are shown in Figure 5(f), and it can be seen that only ZnO was detected, with no other phase present, indicating that Al substitutes fully into the ZnO lattice, in agreement with literature data [2,47]. Moreover, no significant shift in the main ZnO peak (2θ = 36.26 ^{o}) was observed, despite the difference in the ionic radius between Al^{3+} and Zn^{2+} (0.54 vs. 0.74 Å); this can be explained considering the relatively low concentration of the dopant (1-2 mol%), which was not enough to cause significant changes in the ZnO lattice. Indeed, similar behaviour was already reported in Al-doped ZnO materials prepared with different methodologies [54].

ICP analysis confirmed the presence of the aluminium in the samples; more specifically concentrations of 1.17 and 2.48 mol / mol Zn % were detected for **ZnAl1** and **ZnAl2** respectively. These values are slightly lower than the concentrations in the solution used for the aerosol infiltration (see Table 5); nevertheless, this confirms the suitability of this method to incorporate dopants into the ZnO lattice. Regarding the FTIR spectrum of the Al-doped samples, peaks associated with carbon-oxygen bonds can be observed at about 1000 and 1100 cm^{-1}, indicating the presence of some residual organic fragments in the powder (see Figure S9(b)). The UV-Vis spectra, on the other hand, did not present any significant difference in comparison with the undoped samples (data not shown), with no effect observed on the band gap value (3.25 vs. 3.27 eV, i.e. within the experimental error).

However, considering the photocatalytic behaviour of these samples (Figure 8(d)), a significant effect can be seen due to the presence of the aluminium. For **ZnAl1**, a small decrease in the photocatalytic efficiency is observed in comparison with the undoped sample (6.9% vs. 7.7%, respectively). Increasing the dopant concentration to 2 mol% led to an almost complete disappearance of the photocatalysis (**ZnAl2**), as no significant difference could be seen between the decrease in MB with and without light exposure. As already mentioned in the introduction, previous studies already reported a decrease and/or deactivation of the photocatalytic activity for Al-doped ZnO [2,9]; these results are, therefore, in agreement with this. In other cases, however, the opposite effect was observed [54]; these differences can be explained considering that, as stated above, the photocatalytic behaviour can be affected by many factors.

As the material has a white colour, absorbs in the UV range and it does not show photoactivity (with no production of harmful ROS), it has all the features which make it potentially suitable to be used as a sunscreen.

4. Conclusions

ZnO-based materials were successfully prepared using cork as a template agent. The infiltration of the template was performed using for the first time an aerosol; this proved to be effective, as the pyrolysed cork was uniformly infiltrated, even in the small pores present in the cell walls.

The morphology, and hence the functional properties, of the ZnO-based materials were affected by the calcination temperature. In particularly for T = 350 ^{o}C the material showed high capacity of adsorbing and photodegrading MB; these properties were negatively affected by higher calcination temperatures.

Moreover, with the addition of dopants it was possible to tailor the properties of the materials; indeed an enhancement in the photocatalytic activity was observed when Ag was added, while a quenching of the activity was seen with the addition of Al. This made the material suitable to be a sunscreen.

Overall cork showed to be a suitable template agent, which could be used for the preparation of other ecoceramics. The use of aerosol also gave interesting results and it should be further explored, considering for instance different solvents.

Acknowledgements

This work was financially supported by the projects HApECOrk, funded by Fondazione “Con il Sud” (project 2015-0243), and “FutureInResearch” APQ Ricerca Regione Puglia. This work was developed within the scope of the project CICECO-Aveiro Institute of Materials, FCT Ref. UID/CTM/50011/2019, financed by national funds through the FCT/MCTES. The authors wish

to thank Ms. Stefania D'Amone for the help with SEM microscopy. R.C. Pullar thanks FCT grant IF/00681/2015 for supporting this work, and R.M. Novais wishes to thank FCT project H2CORK (PTDC/CTM-ENE/6762/2014). The authors also acknowledge Amorim Cork Composites for providing the cork samples.

References

[1] P. Zhu, Z. Weng, X. Li, X. Liu, S. Wu, K.W.K. Yeung, X. Wang, Z. Cui, X. Yang, P.K. Chu, Biomedical applications of functionalised ZnO nanomaterials: from biosensors to bioimaging. Adv Mater. Inter. 3 (2016) 1500494.

[2] D.V. Dao, M. van den Bremt, Z. Koeller, T.K. Le, Effect of metal ion doping on the optical properties and the deactivation of photocatalytic activity of ZnO nanopowder for application in sunscreen. Powd. Tech. 288 (2016) 366-370.

[3] T.T. Ali, K. Narasimharao, I.P. Parkin, C.C. Carmalt, S. Sathasivam, S.N. Basahel, S.M. Bawaked, S.A. Al-Thabaiti, Effect of pretreatment temperature on the photocatlysic activity of microwave irradiated porous nanocrystalline ZnO. New J. Chem. 39 (2015) 321-332.

[4] K. Kairyte, A. Kadys, Z. Luksiene, Antibacterial and antifungal activity of photoactivated ZnO nanoparticles in suspension. J. Photochem. Photobiol. B 128 (2013) 78-84.

[5] N. Güy, M. Özacar, The influence of noble metals on photocatalysis. Int. J. Hydrog. Ener. 41 (2016) 20100-20112.

[6] R. Pagano, A. Quarta, S. Pal, A. Licciulli, L. Valli, S. Bettini, Enhanced solar-driven applications of ZnO@Ag patchy nanoparticles. J. Phys. Chem. C 121 (2017) 27199-27206.

[7] W. He, H.K. Kim, W.G. Wamer, D. Melka, J.H. Callahan, J.J. Yin, Photogenerated charge carriers and reactive oxygen species in ZnO/Au hybrid nanostructures with enhanced photocatalytic and antibacterial activity. J. Amer. Chem. Soc. 136 (2014) 750-757.

[8] C.B. Ong, L.Y. Ng, A.W. Mohammad, A review of ZnO nanoparticles as solar photocatalysts: synthesis, mechanisms and applications. Renew. Sust. Ener. Rev. 81 (2018) 536-551.

[9] J.D.L. Andrade, A.G. Oliveira, V.V.G. Mariucci, A.C. Bento, M.V. Companhoni, C.V. Nakamura, S.M. Lima, L.H.D.C. Andrade, J.C.G. Morares, A.A.W. Hechenleitner, E.A.G. Pineda, D.M.F. de Oliveira, Effects of Al^{3+} concentration on the optical, structural, photocatalytic and cytotoxic properties of Al-doped ZnO. J. All. Comp. 729 (2017) 978-987.

[10] O. Paris, G. Fritz-Popovski, D. Van Opdenbosch, C. Zollfrank, Recent progress in the replication of hierarchical biological tissues. Adv. Funct. Mater. 23 (2013) 4408-4422.

[11] A. Tampieri, S. Sprio, A. Ruffini, G. Celotti, I.G. Lesci, N. Roveri, From wood to bone: multi-step process to convert wood hierarchical structures into biomimetic hydroxyapatite scaffolds for bone tissue engineering. J. Mater. Chem. 19 (2009) 4973-4980.

[12] M. Singh, J. Martínez-Fernández, A.R. de Arellano-López, Environmentally conscious ceramics (ecoceramics) from natural wood precursors, Curr. Op. Solid State Mater. Sci. 7 (2003) 247-254.

[13] M. Demertzi, J. Amaral, P.L. Arroja, A.C. Dias, A carbon footprint simulation model for the cork oak sector. Sci. Tot. Env. 566-567 (2016) 499-511.

[14] H. Pereira, The rationale behind cork properties: A review of structure and chemistry. Biores. 10 (2015) 1-23.

[15] K. Triantou, B. Perez, A. Marinou, S. Florez, K. Mergia, G. Vekinis, J. Barcena, W. Rotärmel, C. Zuber, d À.e Montbrun, Performance of cork and ceramic matrix composite joints for re-entry thermal protection structures. Compos. B 108 (2017) 270-278.

[16] R.C. Pullar, P. Marques, J. Amaral, J.A. Labrincha, Magnetic wood-based biomorphic $Sr_3Co_2Fe_{24}O_{41}$ Z-type hexaferrite ecoceramics made from cork template. Mater. Des. 82 (2015) 297-303.

[17] R.C. Pullar, R.M. Novais, Ecoceramics - Cork-based Biomimetic Ceramic 3-DOM Foams, Mater. Today 20 (2017) 45-46.

[18] V.O. Yukhymchuk, V.S. Kiselov, M.Y. Valakh, M.A. Skoryk, A.G. Rozhin, S.A. Kulinich, A.E. Belyaev, Biomorphous SiC ceramics prepared from cork oak as precursor. J. Phys. Chem. Sol. 91 (2016) 145-151.

[19] S.P. Silva, M.A. Sabino, E.M. Fernandes, V.M. Correlo, L.F. Boesel, R.L. Reis, Cork: properties, capabilities and applications, Int. Mater. Rev. 50 (2005) 345-365.

[20] P. Marchand, I.A. Hassan, I.P. Parkin, C.J. Carmalt, Aerosol-assisted delivery of precursors for chemical vapour deposition: expanding the scope of CVD for materials fabrication. Dalton Trans. 42 (2013) 9406-9422.

[21] S. Chen, R.M. Wilson, R. Binions, Synthesis of highly surface-textured ZnO thin films by aerosol assisted chemical vapour deposition. J. Mater. Chem. A 3 (2015) 5794-5797.

[22] R.M. Abdelhameed, D.M. Tobaldi, M. Karmaoui, Engineering highly effective and stable nanocomposite photocatalyst based on NH_2-MIL-125 encirclement with Ag_3PO_4 nanoparticles. J. Photochem. Photobiol. A 351 (2018) 50-58.

[23] X. Hou, K.L. Choy, Processing and Applications of Aerosol Assisted Chemical Vapor Deposition. Chem. Vap. Depos. 12 (2006) 583-596.

[24] R.G. Palgrave, Chemical Vapour Deposition of Nanoparticulate and Nanocomposite Thin Films. PhD thesis (2007).

[25] V. Migliorati, G. Chillemi, P. Dangelo, On the solvation of the Zn^{2+} in methanol: a combined quantum mechanics, molecular dynamics, and EXAFS approach. Inorg. Chem. 50 (2011) 8509-8515.

[26] R.M. Novais, A.P.F. Caetano, M.P. Seabra, J.A. Labrincha, R.C. Pullar, Extremely fast and efficient methylene blue adsorption using eco-friendly cork and paper waste-based activated carbon adsorbent. J. Clean. Prod. 197 (2018) 1137-1147.

[27] W. Song, R. Brugge, I.G. Theodoru, A.L. Lim, Y. Yang, T. Zhao, C.H. Burgess, I.D. Johnson, A. Aguadero, P.R. Shearing, D.J.L. Brett, F. Xie, D.J. Riley, Enhancing distorted metal-organic framework-derived ZnO as anode material for lithium storage by the addition of Ag_2S quantum dots. ACS Appl. Mater. Interf. 9 (2017) 37823-37831.

[28] M. Kruk, M. Jaroniec, Gas adsorption characterization of ordered organic-inorganic nanocomposite materials. Chem. Mater. 13 (2001) 3169-3183.

[29] S. Bettini, R. Pagano, V. Bonfrate, E. Maglie, D. Manno, A. Serra, L. Valli, G. Giancane, Promising piezoelectric properties of new ZnO@Octadecylamine adduct. J. Phys. Chem. C 119 (2015) 20143-20149.

[30] P. Khanra, C.N. Lee, T. Kuila, N.H. Kim, M.J. Park, J.H. Lee, 7,7,8,8-tetracyanoquinodimethane-assisted one-step electrochemical exfoliation of graphite and its performance as an electrode material. Nanosc. 6 (2014) 4864-4873.

[31] W. Yu, M. Brown, N.J.D. Graham, Prevention of PVDF ultrafiltration membrane fouling by coating MnO_2 nanoparticles with ozonation. Scient. Rep. 6 (2016) 30144.

[32] Y. Zhang, X. Xu, L. Cao, Y. Sik Ok, X. Cao, Characterization and quantification of electron donating capacity and its structure dependence in biochar derived from three waste biomasses. Chemosph. 211 (2018) 1073-1081.

[33] A.R. Prasad, P.R. Ammal, A. Joseph, Effective photocatalytic removal of different dye stuffs using green synthesized zinc oxide nanogranules. Mater. Res. Bull. 102 (2018) 116-121.

[34] M. Kahouli, N. Tounsi, N. Mzabi, H. Guermazi, S. Guermazi, Enhanced structural and optical properties of ZnO nanopowder with tailored visible luminescence as a function of sodium hydroxide to zinc sulfate mass ratio. Adv. Powd. Tech. 29 (2018) 325-332.

[35] A.J. Reddy, M.K. Kokila, H. Nagabhushana, J.L. Rao, C. Shivakumara, B.M. Nagabhushana, R.P.S. Chakradhar, Combustion synthesis, characterization and Raman studies of ZnO nanopowders. Spectroch. Acta A 81 (2011) 53-58.

[36] S. Wi, S.J. Chang, S.G. Jeong, J. Lee, T. Kim, K.W. Park, D.R. Lee, S. Kim, Evaluation of toluene adsorption performance of mortar adhesive using porous carbon material as adsorbent. Mater. 10 (2017) 853.

[37] B. Cardoso, A.S. Mestre, A.P. Carvalho, J. Pires, Activated carbon derived from cork powder waste by KOH activation: preparation, characterization, and VOC adsorption. Ind. Eng. Chem. Res. 47 (2008) 5841-5846.

[38] A.S. Mestre, R.A. Pires, I. Aroso, E.M. Fernandes, M.L. Pinto, R.L. Reis, M.A. Andrade, J. Pires, S.P. Silva, A.P. Carvalho, Activated carbon from industrial pre-treated cork: Sustainable adsorbents for pharmaceutical compounds removal. Chem. Eng. J. 253 (2014) 408-417.

[39] X. Yue, R. Zhang, H. Wang, F. Zhang, Sorption and decomposition of crude oil using exfoliated graphite/ZnO composites. J. Phys. Chem. Sol. 70 (2009) 1391-1394.

[40] J. de Sousa Macedo, N.B. da Costa Junior, L.E. Almeida, E.F. da Silva Vieira, A.R. Cestari, I. De Fatima Gimenez, N.L. Villarreal Carreño, L. Silva Barreto, kinetic and calorimetric study of the adsorption of dyes on mesoporous activated carbon prepared from coconut coir dust. J. Coll. Interf. Sci. 298 (2006) 515-522.

[41] M. Rad, S. Dehghanpour, ZnO as an efficient nucleating agent and morphology template for rapid, facile and scalable synthesis of MOF-46 and ZnO@MOF-46 with selective sensing properties and enhanced photocatalytic activity. RSC Adv., 6 (2016) 61784-61793.

[42] W. Raza, S.M. Faisal, M. Owais, D. Bahnemann, M. Muneer, Facile fabrication of highly efficient modified photocatalyst with enhanced photocatalytic, antibacterial and anticancer activity. RSC Adv., 6 (2016) 78335-78350.

[43] M.J. Sampaio, M.J. Lima, D.L. Baptista, A.M.T. Silva, C.G. Silva, J.L. Faria, Al-loaded ZnO materials for photocatalytic water treatment. Chem. Eng. J 318 (2017) 95-102.

[44] S. Verma, R-K. Dutta, Enhanced ROS generation by ZnO-ammonia modified grapheme oxide nanocomposites for photocatalytic degradation of trypan blue dye and 4-nitrophenol. J. Env. Chem. Eng. 5 (2017) 4776-4787.

[45] S. Demirci, M. Yurddaskal, T. Dikici, C. Sariogiu, Fabrication and characterization of novel iodine doped hollow and mesoporous hematite (Fe_2O_3) particles derived from sol-gel method and their photocatalytic performances. J. Haz. Mater. 345 (2018) 27-37.

[46] E.M. Nigri, A. Bhatnagar, S.D.F. Rocha, Thermal regeneration process of bone char used in the fluoride aqueous solution. J. Clean. Prod. 142 (2017) 3558-3570.

[47] Y. Zhao, J. Ma, J. Liu, Y. Bao, Synthesis of fireworks-shaped ZnO/graphite-like carbon nanowires with enhanced visible-light photocatalytic activity and anti-corrosion. Coll. Surf. A 518 (2017) 57-63.

[48] S.S. Türkyilmaz, N. Güy, M. Özacar, Photocatalytic efficiencies of Ni, Mn, Fe and Ag doped ZnO nanostructures synthetized by hydrothermal method: The synergistic/antagonistic effect between ZnO and metals. J. Photochem. Photobiol. A 341 (2017) 39-50.

[49] V. Vaiano, M. Matarangolo, J.J. Murcia, H. Rojas, J.A. Navío, M.C. Hidalgo, Enhanced photocatalytic removal of phenol from aqueous solutions using ZnO modified with Ag. Appl. Catal. B 225 (2018) 197-206.

[50] B. Chai, X. Wang, S. Cheng, H. Zhou, F. Zhang, One-pot triethanolamine-assisted hydrothermal synthesis of Ag/ZnO heterostructure microspheres with enhanced photocatalytic activity. Ceram. Int. 40 (2014) 429-435.

[51] A.K. Pal, B. Mohan, Study of NBE emission enhancement with an absence of DL emission from ZnO nanorods through controlled growth on ultra-thin Ag films. Appl. Surf. Sci. 333 (2015) 244-253.

[52] C. Jaramillo-Páez, J.A. Navío, M.C. Hidalgo, Silver-modified ZnO highly UV-photoactive. J. Photochem. Photobiol. A 356 (2018) 112-122.

[53] R. Dhahri, S.G. Leonardi, M. Hjiri, L. El Mir, A. Bonavita, N. Donato, D. Iannazzo, G. Neri, Enhanced performance of novel calcium/aluminum co-doped zinc oxide for CO_2 sensors. Sens. Actuat. B 239 (2017) 36-44.

[54] Z. Peng, D. Wu, W. Wang, F. Tan, X. Wang, J. Chen, X. Qiao, Effect of metal ion doping on ZnO nanopowders for bacterial inactivation under visible-light irradiation. Powd. Tech. 315 (2017) 73-80.

Table 1. Weight uptake of the pyrolysed cork powder with different numbers of infiltrations.

	Number of infiltration(s)	Weight uptake (g/g)
Zinc acetate	1	1.70 ± 0.51
	2	6.71 ± 1.12
	3	7.20 ± 1.57
Zinc nitrate	1	4.52 ± 0.35
	2	9.60 ± 1.02
	3	14.12 ± 0.55

Table 2. List of single-phase ZnO samples prepared. The heating ramp was a1ways 1 ºC/min.

Sample name	Number of infiltrations	Calcination conditions
ZnAc1	2	350 ºC, 1 hour
ZnAc2	3	350 ºC, 1 hour
ZnAc3	2	400 ºC, 1 hour
ZnAc4	3	400 ºC, 1 hour
ZnAc5	2	350 ºC, 3 hours
ZnAc6	2	350 ºC, 5 hours
ZnAc7	2	350 ºC, 7 hours
ZnNit1	2	350 ºC, 1 hour
ZnNit1a	2	Second calcination at 700 ºC, 1 hour
ZnNit2	3	350 ºC, 1 hour
ZnNit3	2	400 ºC, 1 hour
ZnNit4	3	400 ºC, 1 hour
ZnNit5	2	350 ºC, 3 hours
ZnNit6	2	350 ºC, 5 hours
ZnNit7	2	350 ºC, 7 hours

Table 3. Crystallite size of the single-phase ZnO samples.

Sample name	Crystallite size (nm)
ZnAc1	13.88 ± 0.14
ZnAc2	13.95± 0.15
ZnAc3	14.43 ± 0.14
ZnAc4	14.61 ± 0.15
ZnAc5	14.05 ± 0.14
ZnAc6	14.31 ± 0.14
ZnAc7	13.95 ± 0.14
ZnNit1	16.52 ± 0.17
ZnNit1a	22.47 ± 0.23
ZnNit2	16.71 ± 0.17
ZnNit3	17.82 ± 0.19
ZnNit4	17.99 ± 0.18
ZnNit5	16.29 ± 0.16
ZnNit6	16.82 ± 0.17
ZnNit7	17.20 ± 0.17

Table 4. List of the doped ZnO samples.

Sample name	Dopant concentration (mol/mol Zn %)
Ag doping	
ZnAg1	1
ZnAg2	2
ZnAg3	3
ZnAg4	5
Al doping	
ZnAl1	1.5
ZnAl2	2.5

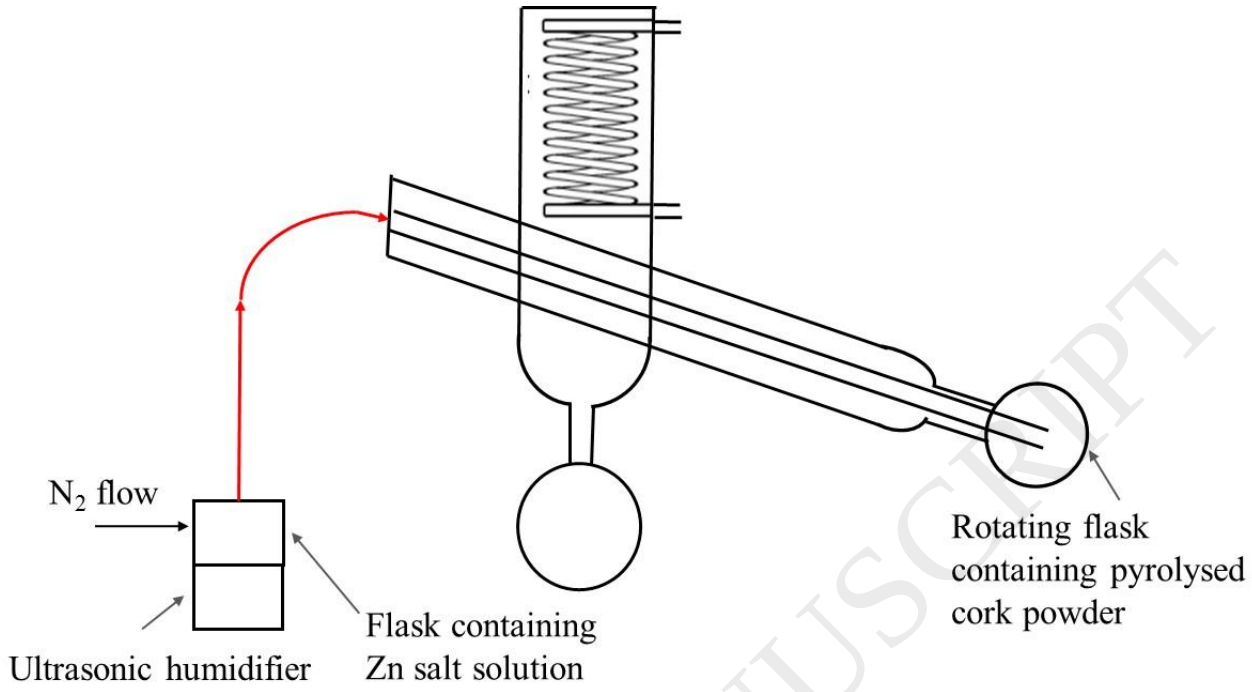

Figure 1. Apparatus used for the aerosol impregnation of pyrolysed cork powder.

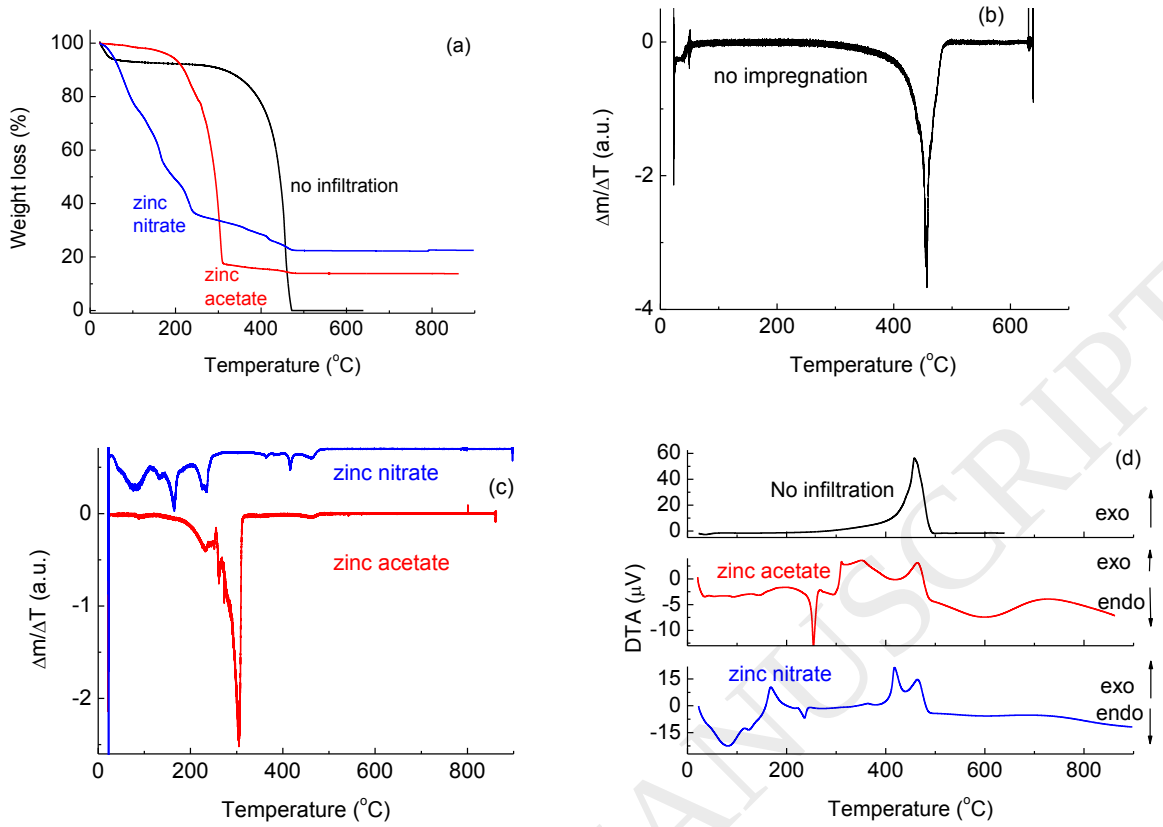

Figure 2. TGA-DTA data. (a) TGA curves of non-infiltrated powders, and zinc acetate and zinc nitrate infiltrated powders; (b) first derivative of the TGA of the non-infiltrated powder; (c) first derivative of the TGA of zinc acetate and zinc nitrate infiltrated powders; (d) DTA curves.

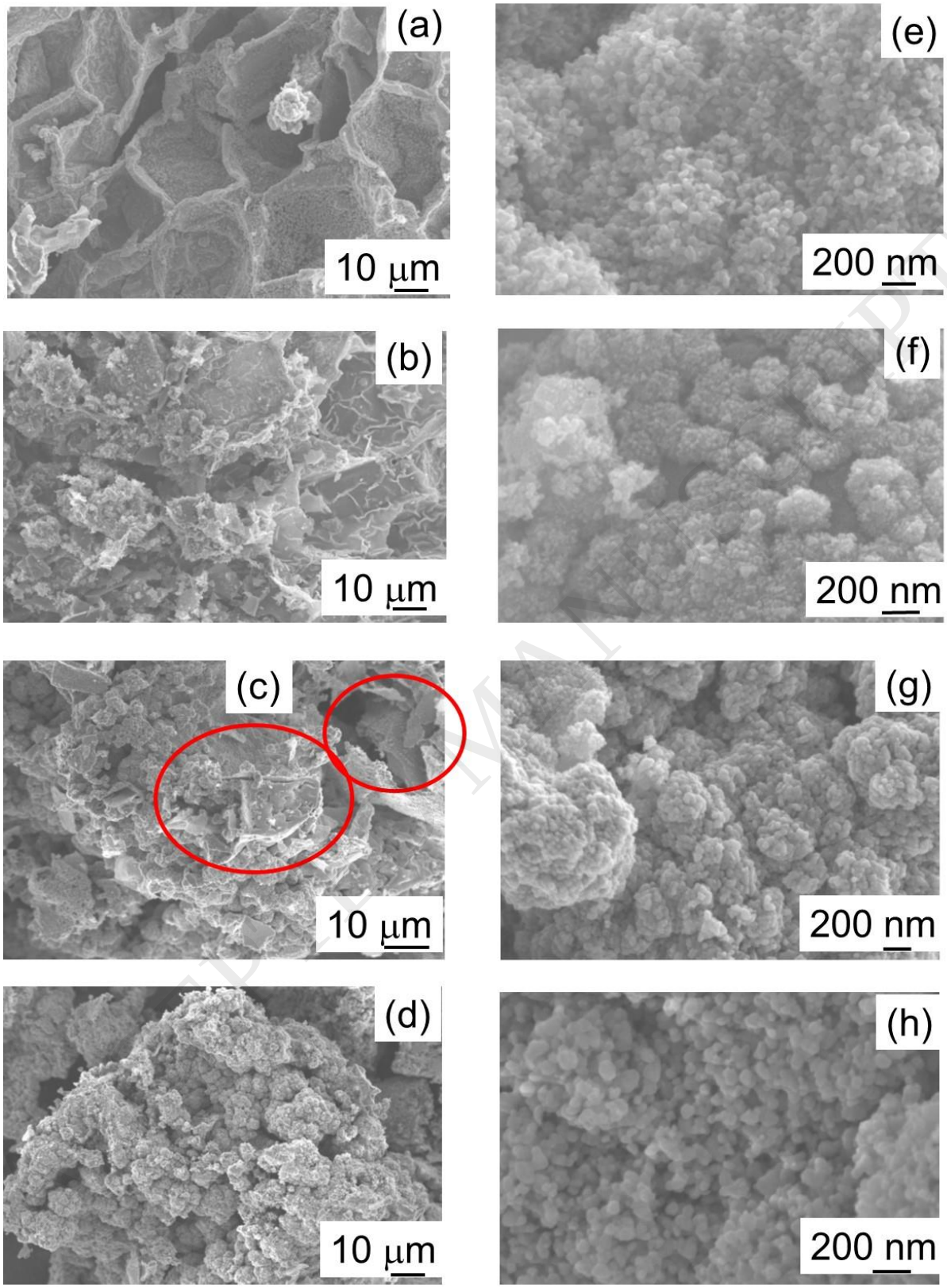

Figure 3. SEM images of sample (a,e): **ZnAc1**, (b,f) **ZnAc2**, (c,g) **ZnAc3**, (d,h) **ZnAc4**. The circles in Figure 3(c) indicate areas that could correspond to burnt cell walls.

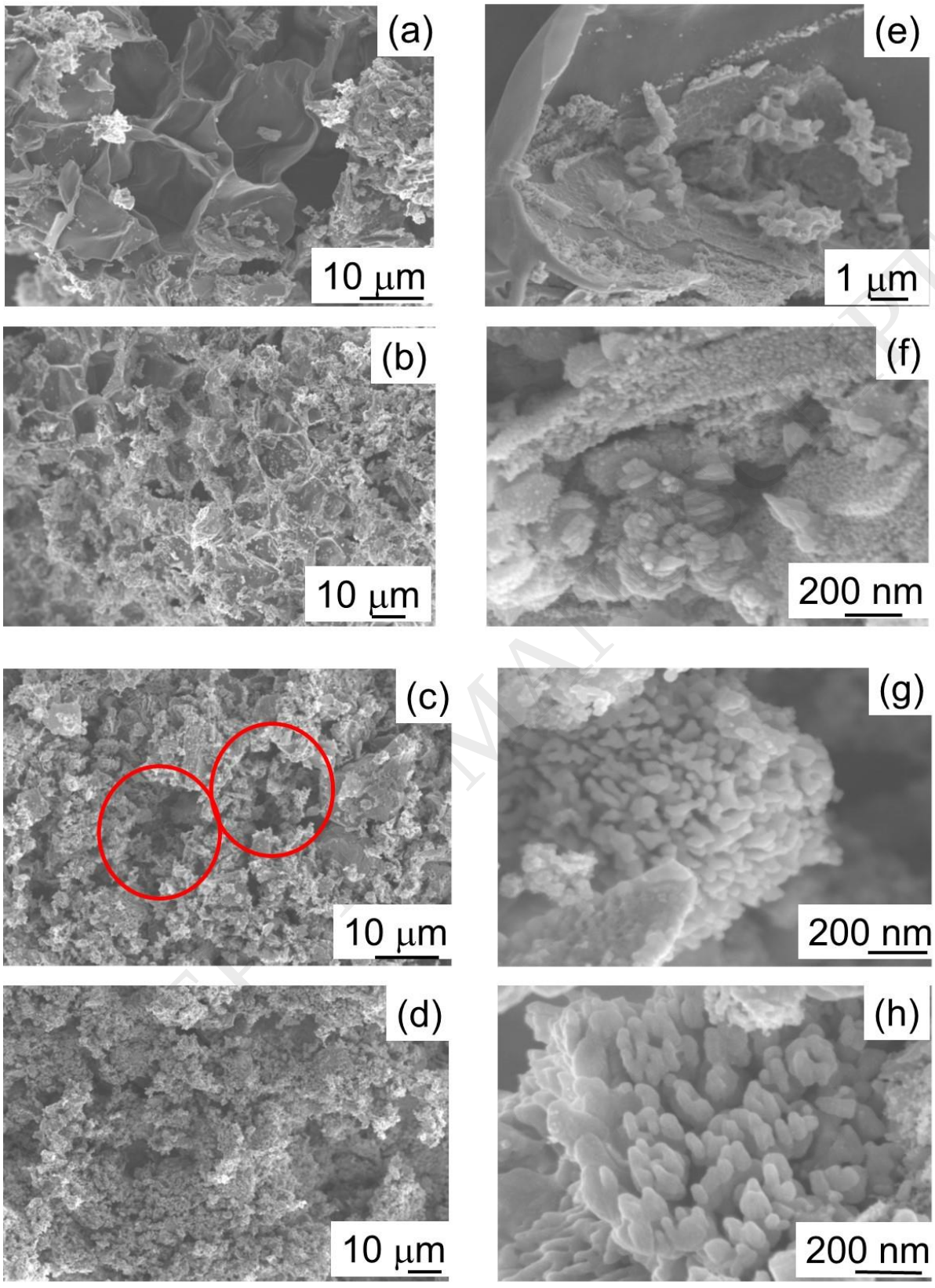

Figure 4. SEM images of sample (a,e): **ZnNit1**, (b,f) **ZnNit2**, (c,g) **ZnNit3**, (d,h) **ZnNit4**. The circles in Figure 4(c) show empty voids which could derive from cork cells.

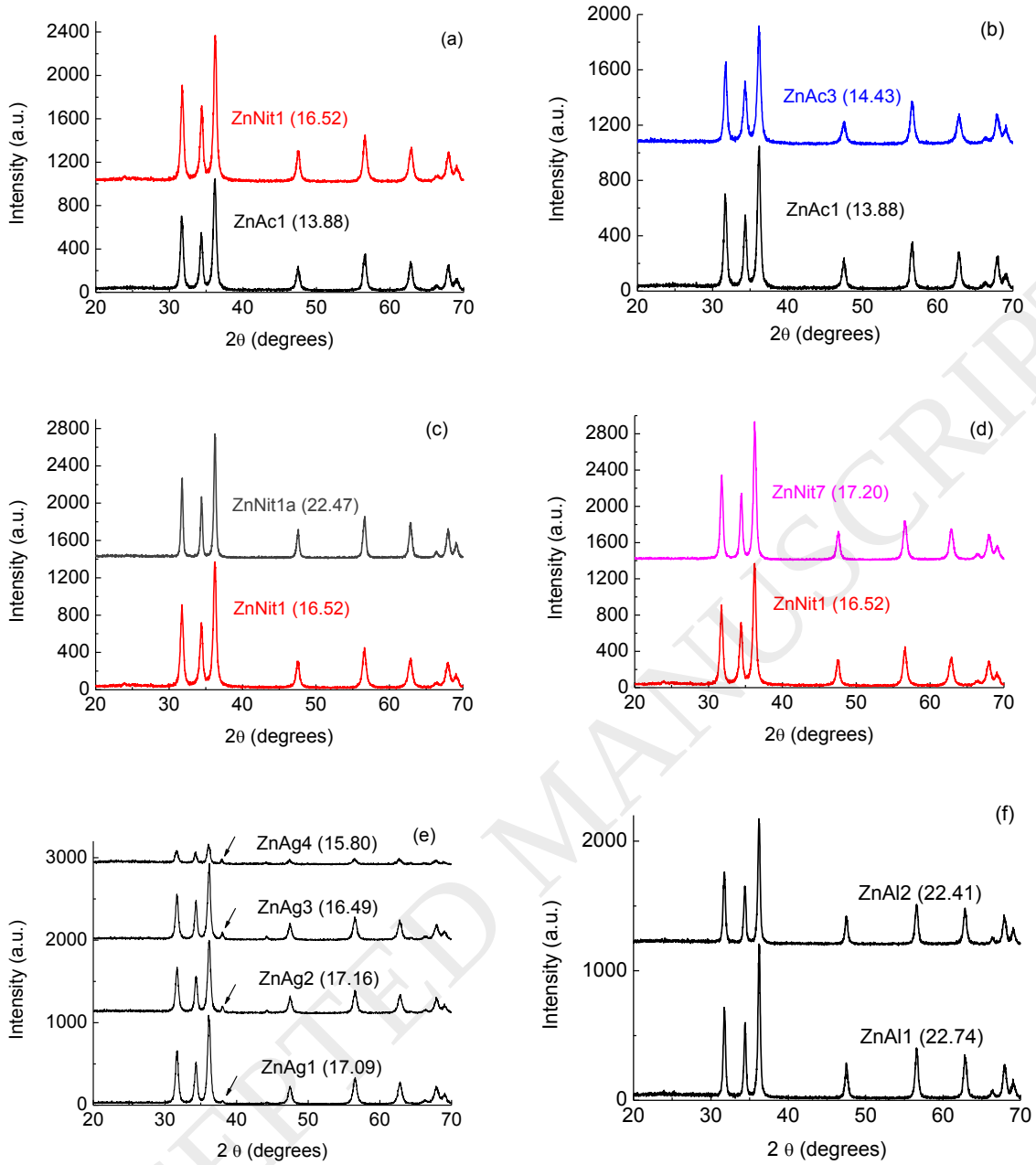

Figure 5. XRD patterns (a-d) of selected undoped (e) Ag-doped and (f) Al-doped ZnO samples. (a) Acetate vs. nitrate using the same preparation conditions; (b) acetate at two different calcination temperature (350 and 400 ^{o}C); (c) same nitrate sample calcined at 350 ^{o}C and then recalcined at 700 ^{o}C; (d) nitrate calcined at 350 ^{o}C for different lengths of time (1 and 7 hours); (e) samples with different Ag concentration, the arrow indicates the Ag peak; (f) samples with different Al concentration.

The number in brackets indicates the value of the crystallite size (nm).

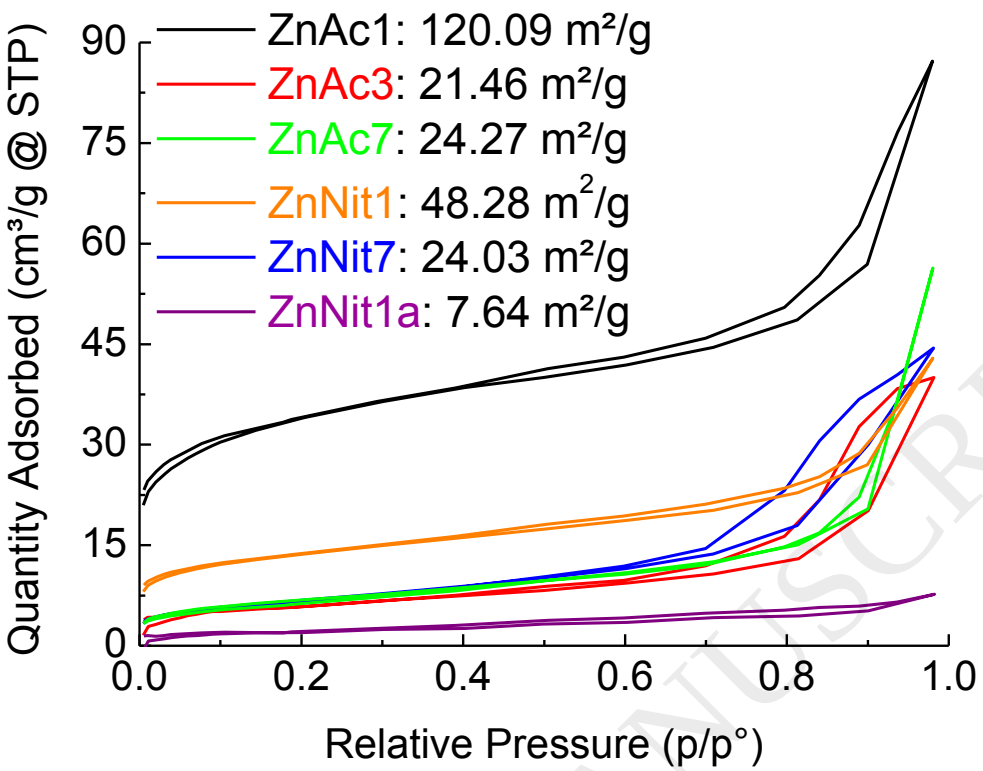

Figure 6. BET isotherms and SSA values of selected samples.

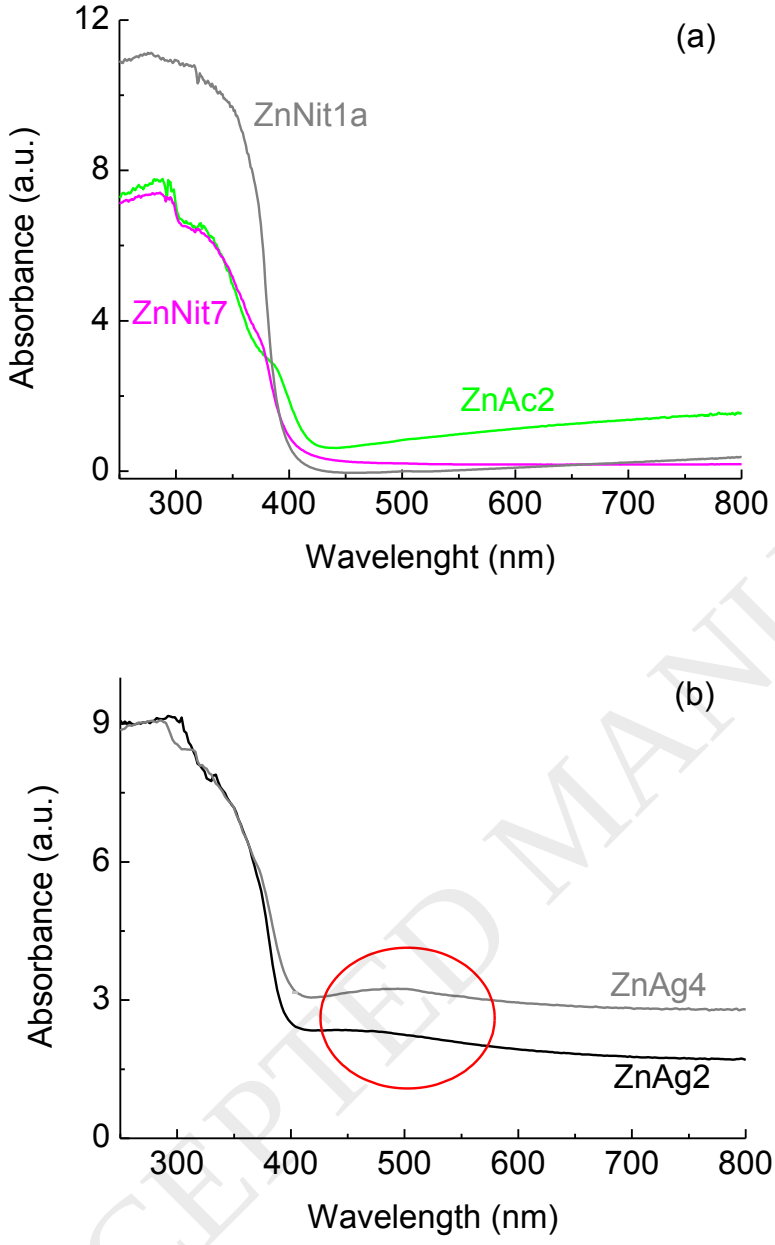

Figure 7. UV-Vis absorption spectra of some selected ZnO samples.

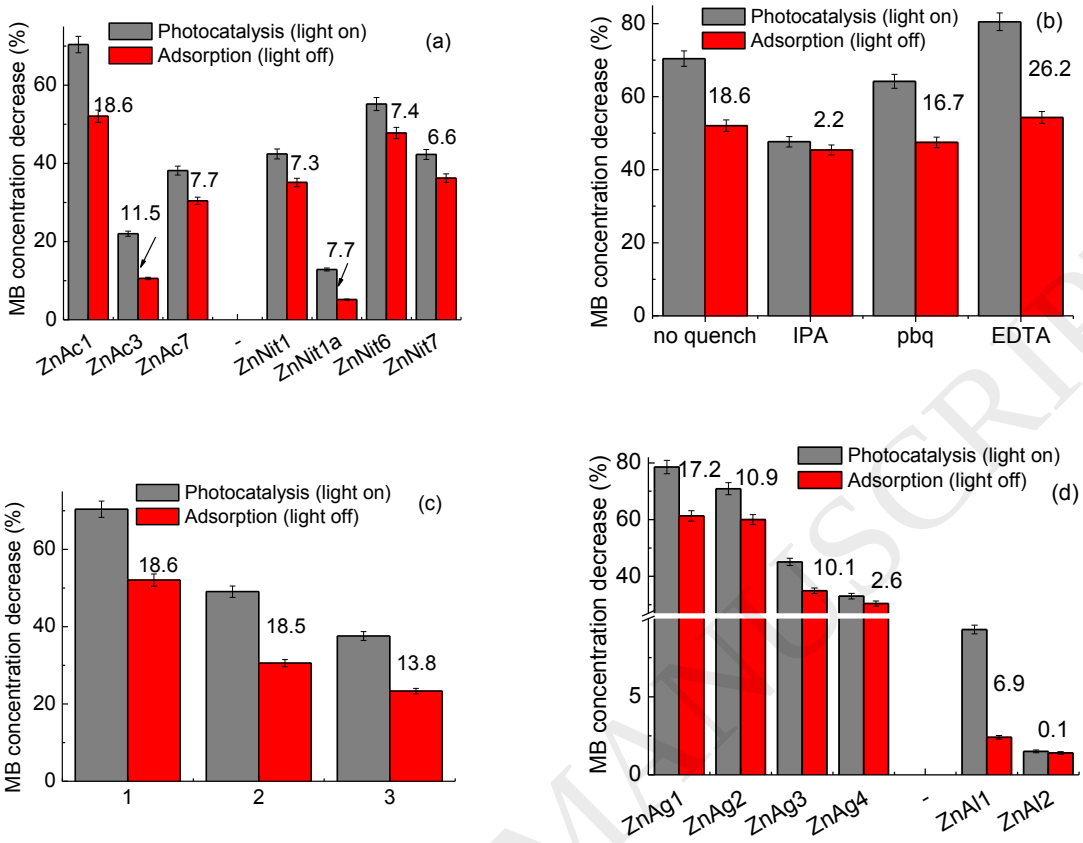

Figure 8. Photocatalytic activity of some selected ZnO samples. (a) Tests for different undoped ZnO samples; (b) Test for ZnAc1 sample in presence of different quenchers; (c) repeated tests for ZnAc1 sample; (d) tests for doped ZnO samples. Black columns: tests performed under light irradiation; red columns: tests performed in the dark. The numbers in the figure represent the difference in MB concentration decrease between the two tests (with and without light) for each sample, i.e. the decrease in MB concentration due to photocatalysis only.